Aparicio Esteve, E., Hernández Alonso, Á. & Ureña Ureña, J. 2021, "Design, Calibration, and Evaluation of a Long-Range 3-D Infrared Positioning System Based on Encoding Techniques", IEEE Transactions on Instrumentation and Measurement, vol. 70, art. no. 7005113, pp. 1-13.

Available at http://dx.doi.org/10.1109/TIM.2021.3089223

Design, Calibration and Evaluation of a long-range 3D Infrared Positioning System based on Encoding Techniques

Elena Aparicio-Esteve, Álvaro Hernández, Jesús Ureña
Electronics Department, *University of Alcalá*
Alcalá de Henares (Madrid), Spain
{elena.aparicio, alvaro.hernandez, jesus.urena}@uah.es

***Abstract*—Optical indoor positioning systems have experienced an increasing research interest during last years as they can provide 3D centimeter accuracy using LED lighting. In the case of having several LEDs emitting simultaneously and a receiver (e.g. the tag to be localized), these systems face important challenges, such as very high dynamic ranges with low Signal-to-Noise Ratios when the coverage area is increased, Multiple Access Interference (MAI), multipath and near-far effects, calibration issues (misalignments in the receiver and other intrinsic parameters), and so on. Previous work have already shown the feasibility of using LED emitters in combination with Quadrature Angular Diversity Aperture (QADA) receivers to implement positioning systems. This work further introduces new design considerations, tested on an experimental setup, to enlarge the emitter-receiver range, thus increasing the total coverage, while dealing with the aforementioned challenges. The system applies encoding techniques to each transmitter to solve the multiple access problem. The performance of two different types of codes has been compared, as well as their influence on the final estimation of the receiver's position: one based on Kasami sequences and another based on Loosely Synchronous (LS) codes, derived from Complementary Sets of Sequences. At the receiver, the estimation of the incident point is constrained to angles at which the system can be linearized, and a specific calibration process for this type of sensor has also been defined and applied. The proposal has been finally validated with both, simulated and experimental results, in a large space of $2 \times 2\,\mathrm{m}^2$ (base), with a distance from transmitters to receiver of $3.4\,\mathrm{m}$ (height). The experimental tests at distances up to $4\,\mathrm{m}$, carried out after the calibration process, achieve average absolute errors bellow $10\,\mathrm{cm}$ for X and Y axis and around $20\,\mathrm{cm}$ for Z, and standard deviations below $4\,\mathrm{cm}$ for X and Y, and around $30\,\mathrm{cm}$ for Z.**

***Index Terms*—Indoor 3D local positioning systems (LPS), QADA receiver, encoding techniques, infrared sensors.**

I. Introduction

There is a current need on improving local indoor localization in places where Global Navigation Satellite Systems (GNSS) signals do not have the necessary strength to overcome the issues coming from attenuation and multipath effect that limit their behaviour in indoor environments. Several approaches have been developed throughout the last decade to overcome those weaknesses, based on optical, mechanical, acoustic, and radio-frequency signals, among others [1]. In recent years, there has been a particular interest in positioning with optical signals due to the massive use of the LED (Light Emitting Diode) technology, which has low cost, long lifetime and broad distribution in the vast majority of homes, building and indoor spaces [2].

Both Infrared and Visible Light Local Positioning Systems (IRLPS and VLPS) typically use triangulation as the positioning technique in their algorithms. In particular, some work rely on Angle-of-Arrival (AoA) measurements in order not to deal with the velocity of light when using Time-of-Flight (ToF) (or Time-of-Arrival, ToA; Time-Difference-of-Arrival, TDoA) measurements [3]. Furthermore, this approach does not require either an exhaustive analysis of the light reflections and the multipath effect, which are necessary whether Received Signal Strength (RSS) measurements are involved [4].

Common receivers can be divided into those based on cameras [5] and those based on photodiodes [6]. Positioning systems based on cameras usually require complex image processing algorithms that slow down the positioning computation [7]. On the other hand, those whose receptor is a photodiode typically combine it with lenses or with apertures in order to reach longer distances. The photodiodes in combination with apertures also face some unresolved challenges. One of them is the design of the aperture to be placed on the sensor. Furthermore, these systems tend to use complicated structures using arrays with several apertures and different shapes [8] [9] [10]. All these systems often have boundary problems due to non-linear responses that are hard to manage, and imply some approximations that deteriorate the system performance. Other significant issue that requires more research in coming years is the medium access technique, often related to the modulation and/or encoding scheme used in the transmissions, which allows the receiver to easily identify each transmission while providing a robust link.

Most previous work use an On-Off-Keying (OOK) modulation [11] due to its simplicity [12], whereas others apply a Pulse Position Modulation (PPM) [13], since it is the most robust modulation against Inter-Symbol Interference (ISI), together with the Pulse Width Modulation (PWM). On the

This work has been supported by the Spanish Ministry of Science,Innovation and Universities (MICROCEBUS project, ref. RTI2018-095168-BC51, and POM project, ref. PID2019-105470RA-C33), the Community of Madrid (PUILPOS project, ref. CM/JIN/2019-038 and CODEUS project, ref. CM/JIN/2019-043) and the Youth Employment Program (ref. PEJ2018-003459-A).

other hand, in [14] a Binary Phase Shift Keying (BPSK) modulation is compared with an OOK modulation, resulting in the first one to have the best performance in visible light communications.

The encoding of the emitted light signals is key to identify each transmitter in Code Division Multiple Access (CDMA) systems. Some applications have already proposed encoding schemes that allow simultaneous interference-free transmissions. Since Barker and Walsh codes cannot provide several sequences with low cross-correlation functions or they require a precise synchronism between emitters and receivers [15], in order to overcome these drawbacks, it has been proposed the use of Pseudo-Random sequences (PR), such as Gold [16] or Kasami codes [17], as well as Complementary Sets of Sequences (CSS) or sequences derived from them, such as Loosely Synchronous (LS) codes [18]. It is worth remarking that the encoding technique often has significant influence on the final performance of the system, since, whether simultaneous transmissions are carried out, the Multiple Access Interference (MAI) may imply a systematic error in the position estimates. Furthermore, those sequences with more robust behaviour against MAI often require complex transmission and reception schemes, which might involve longer transmission times and lower position updating rates.

A last aspect to consider is the necessary calibration of the optical setup, mainly the intrinsic parameters of the optical receiver, since undesired misalignments in the experimental setup may lead to high position errors in the range of decimeters, or even meters. One of the most commonly used algorithms in camera calibration is the Zhang Method [19], where several images are taken from a two-dimensional template (e.g., a checkerboard) or from certain tags [20]. Other alternatives are related to Direct Linear Transformation (DLT) [21] or iterative methods [22] to obtain optimized parameters that best fit the model used. Nevertheless, these algorithms cannot be directly applied to the QADA receiver, due to the different structural configuration of the sensor regarding those of the cameras.

In comparison with previous work [23] [24], and considering the challenges aforementioned, this work proposes: a simplification in the estimation of the incident point of light on the QADA sensor by decreasing the size of the aperture and, hence, linearizing the corresponding equations; an analysis of the MAI effect in the proposed system with different sequences to improve the estimation of the receiver's position; and, finally, these studies are underpinned by a successful validation of the proposal in both simulated and experimental tests, thus resulting in a scenario of $2 \times 2\,\mathrm{m}^2$ (base), and a distance from transmitters to the receiver of $3.4\,\mathrm{m}$ (height), longer than previous works. This new experimental setup has been verified by means of a commercial ground-truth solution. The rest of the manuscript is organized as follows: Section II provides a general overview of the proposal; Section III describes the proposed algorithm for the central impact point estimation; Section IV details the encoding sequences considered; Section V shows some simulated results; Section VI deals with the receiver calibration, Section VII provides some experimental results; and, finally, conclusions are discussed in Section VIII.

II. General Overview of the Proposal

The proposed optical positioning system is based on a set of four transmitters placed at certain points in the environment, so that they cover an area where the receiver can detect all the transmissions and, therefore, estimate its position. A general diagram of the proposal is presented in Fig. 1 [17] [24]. Two independent coordinate systems are considered in this proposal: $[X,\ Y,\ Z]$ denotes the global coordinate system whose centre is located in the corner of the room; and $[X_r,\ Y_r,\ Z_r]$ is the local coordinate system of the QADA and its centre is located at the centre of the photoreceiver, with the axes X_r and Y_r aligned with the QADA axes. The pose of the receiver is denoted as $(x,\ y,\ z,\ \beta)$, where β is the rotation angle of the receiver around the vertical axis.

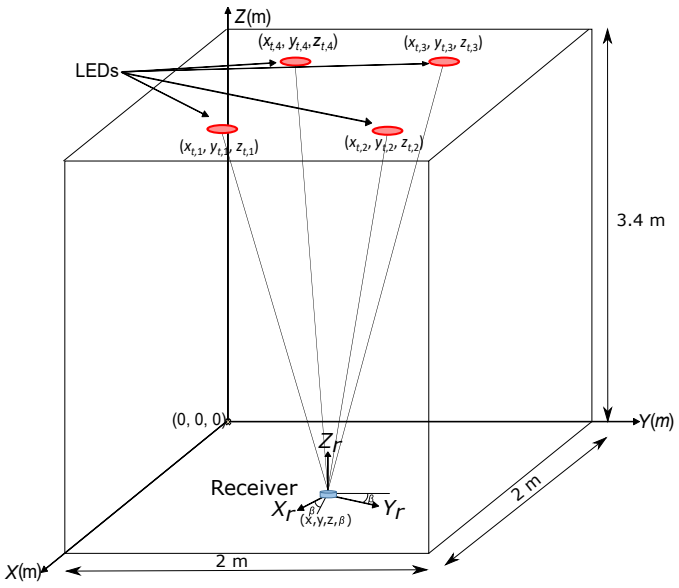

Fig. 1. Global overview of the proposed positioning system.

AoA-based IRLPS or VLPS typically use Line-of-Sight (LoS) measurements to estimate the receiver's position. For that purpose, it is important to successfully detect the entire transmitted sequence without any interference either from reflections in a multipath context, or from Inter-Symbol Interference (ISI) or MAI. Since the positioning algorithm is performed by an identification of the different transmitters in an AoA system, it is required to implement a CDMA technique, where every LED i transmits its own code c_i.

In Fig. 2 the global coverage volume is presented, where the black crosses are the positions of transmitters detailed in Table I and the coloured map represents the maximum height at which the receiver can be placed, while still receiving emissions from the four transmitters with a particular beam angle of $150°$.

The maximum height at which the receiver can be placed is obtained by the estimation of the maximum distance, from the receiver centre, at which the incident wave impacts the photoreceiver after it passes the aperture. This is determined with Matlab©software by using ray tracing from the transmitters to the photoreceiver. We analyze two cases: the most general, in which it is enough that the ray that passes through the

centre of the aperture impacts inside the sensitive area of the photoreceiver and, one more restrictive, in which all the rays passing through the aperture impact on the sensitive area. In this way, for the first case mentioned, when the aperture side is equal to the diameter of the photoreceiver (r = 3.9 mm), the coverage volume is presented in Fig. 2.a). On the other hand, for the sencond case, when using an aperture side length of $l = 2.75\,\mathrm{mm}$ (it will be shown in Section III that this is the maximum size for a linear response of the system), the coverage volume is smaller, as presented in Fig. 2.b). For all the test area, the receiver can be placed at heights from the floor up to 2m (first case) and up to 0.5m (second case).

TABLE I
LED'S COORDINATES CONSIDERED IN SIMULATIONS.

LED i	**Coordinates** ($x_{t,i}$, $y_{t,i}$, $z_{t,i}$)
LED 1	(1.33 m, 0.66 m, 3.40 m)
LED 2	(1.33 m, 1.33 m, 3.40 m)
LED 3	(0.66 m, 1.33 m, 3.40 m)
LED 4	(0.66 m, 0.66 m, 3.40 m)

Concerning the system characterization, for the analysis and measurements conducted in this work, it is considered that transmitters are not rotated nor tilted, but the receiver can have any rotation β in the vertical axis. Besides, in order to properly position the receiver, at least three emitters must be detected in the QADA receiver. Note that, in practical applications, some of these constraints may be released. For instance, the proposed system can be used in its current configuration as a 3D IRLPS to obtain the position and orientation (x, y, z, β) in the XY plane of a robot, moving on a horizontal floor, thus reducing the complexity of estimating the coordinate z.

III. Proposed Estimation of the Central Impact Point at the Receiver

The principle of operation in the proposal is based on the fact that the light coming from the LEDs goes through the square aperture, and lights the QADA photoreceiver (see Fig. 3). Note that the aperture is fully aligned with the QADA sensor, so the centre of the aperture perfectly matches the centre of the QADA. The central point of the illuminated area is of special interest and corresponds to the ray that crosses the center of the aperture.

According to the incidence angle, different areas are illuminated on each one of the different photodiodes. Fig. 4 shows the four quadrants k ={1,2,3,4} and their areas A_k covered by the beam of light that passes through the aperture for the case of an incident ray with a central impact point (x_r, y_r).

The incident light generates four different currents $i_k(t)$ for every quadrant k ={1,2,3,4} that are combined to provide the sum of all quadrant signals (V_{sum}) and two difference signals, bottom minus top for the Y axis (V_{bt}) and left minus right for the X axis (V_{lr}). Note that all quadrants must be illuminated in order to estimate the incident point.

Once these three signals are obtained, the system correlates the acquired signals with the transmitted codes c_i, so that every signal coming from each transmitter can be identified, while minimizing other impairment signals (noise, ambient light,

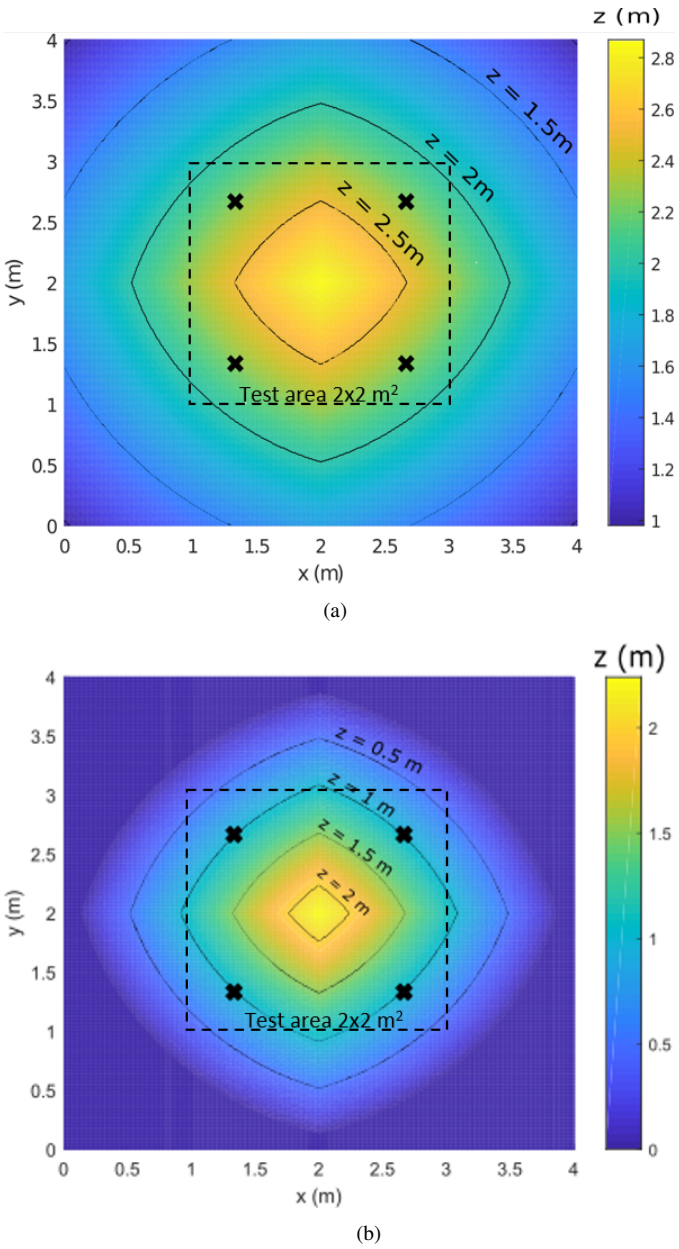

Fig. 2. Coverage particularized for a beam angle $\alpha = 150°$ with the four transmitters at XY planes ($z = \{1.5\,\mathrm{m}, 2\,\mathrm{m}, 2.5\,\mathrm{m}\}$): a) without aperture size constraint; b) with an aperture side length $l = 2.75\,\mathrm{mm}$.

incoming sunlight, etc.). It is worth noting that the receiver detects all the transmitted codes simultaneously. The resulting signals $s_i[n]$, $t_i[n]$ and $r_i[n]$ are the correlation functions of the signals V_{sum}, V_{bt} and V_{lr} with the transmitted codes c_i transmitted by the i-th LED, respectively .

As the photocurrents in the QADA are proportional to the illuminated areas, these can be combined to obtain the ratios p_x and p_y (1) (2).

$$p_x = \frac{V_{lr}}{V_{sum}} = \frac{(A_2 + A_3) - (A_1 + A_4)}{A_1 + A_2 + A_3 + A_4} \tag{1}$$

$$p_y = \frac{V_{bt}}{V_{sum}} = \frac{(A_3 + A_4) - (A_1 + A_2)}{A_1 + A_2 + A_3 + A_4} \tag{2}$$

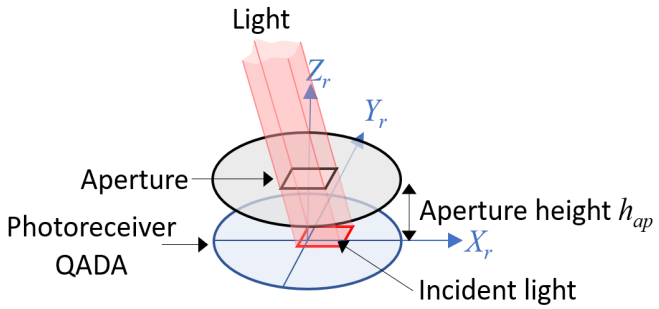

Fig. 3. Geometrical representation of the incident light in the QADA sensor.

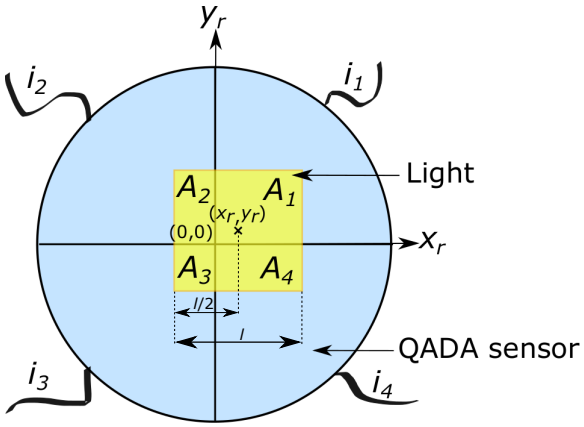

Fig. 4. Representation of the incident light in the QADA sensor.

In Fig. 5 the ratio p_x in (1) is plotted for different sizes of the aperture l. It is worth mentioning that Eqs. (1) and (2) are linear when the illuminated areas A_k in the QADA sensor are always within the photodiodes' areas. This linearity is fulfilled when the diagonal of the used aperture is equal to or smaller than the radius of the QADA (r = 3.9 mm), and, therefore, the side of the aperture is equal to or smaller than $l = \sqrt{\frac{r^2}{2}} = 2.75$ mm, as can be observed in Fig. 5. This analysis can similarly be extended for p_y.

There is a trade-off between minimizing the aperture size and maximizing the FoV (Field-of-View), since a smaller aperture size results in a smaller FoV (see Fig. 2). In particular, for $l = 2.75$ mm, the QADA receiver will only detect angles of incidence lower than 36.87º. Note that diffraction effects are not considered, since the wavelength of the emission is small compared to the aperture side $l = 2.75$ mm.

In order not to have any boundary issue (i.e., non-linearity in the calculation of p_x and p_y), we propose a square aperture, smaller than the one used in previous work [23], which assures that the illuminated areas A_k on the QADA sensor are always confined inside the photodetector's sensitive areas. Eqs. (3) - (6) define the illuminated areas A_k when the central incident point is located at any generic point (x_r, y_r).

$$A_1 = (l/2 + x_r) \cdot (l/2 + y_r) \tag{3}$$

$$A_2 = (l/2 - x_r) \cdot (l/2 + y_r) \tag{4}$$

$$A_3 = (l/2 - x_r) \cdot (l/2 - y_r) \tag{5}$$

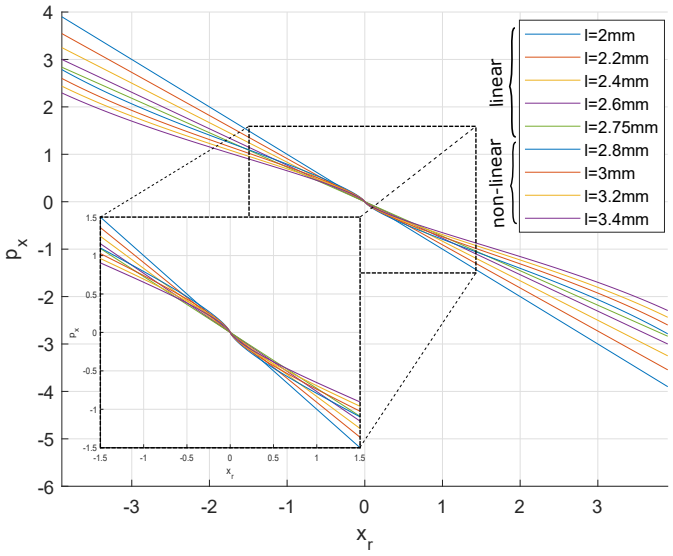

Fig. 5. Representation of the ratio p_x according to the aperture side l for $-r < x_r < r$.

$$A_4 = (l/2 + x_r) \cdot (l/2 - y_r) \tag{6}$$

Combining (1)-(6), the centre of the light incidence can be defined as (7). Note that different terms cancel out so that x_r and y_r only depend on p_x and p_y, respectively.

$$\begin{bmatrix} x_r \\ y_r \end{bmatrix} = \frac{-l}{2} \cdot \begin{bmatrix} p_x \\ p_y \end{bmatrix} \tag{7}$$

A. Analysis of Other Intrinsic Parameters

There are other parameters that have an impact on the estimation of the light incidence centre (x_r, y_r), which are the intrinsic parameters of a pin-hole system. Since the proposed system relies on the accurate location of the aperture onto the QADA receiver, the parameters under consideration are: the optical centre (x_c, y_c), which is defined as the centre of the square aperture placed on top of the QADA receiver; the height h_{ap} at which the aperture is located (in other words, the focal length); the aperture misalignment δ, which is defined as the rotation of the aperture with respect to the photoreceiver axis; and the length of the aperture l (see Fig. 6).

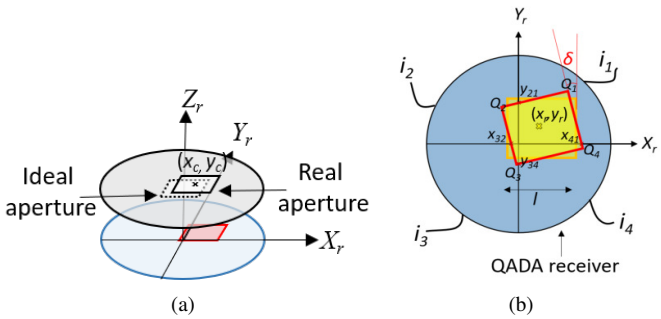

Fig. 6. Parameters to calibrate in the aperture of the QADA: a) optical centre; b) aperture misalignment.

The optical centre (x_c, y_c) and the correction of the focal distance h_{ap} can be adjusted in the central incident point

$\left(\begin{bmatrix} x_{r,\lambda,c} \\ y_{r,\lambda,c} \end{bmatrix}\right)$ according to (8), where λ is the relation between the expected focal length h_{ap} and the actual focal length h'_{ap}: $\lambda = \frac{h'_{ap}}{h_{ap}}$.

$$\begin{bmatrix} x_{r,\lambda,c} \\ y_{r,\lambda,c} \end{bmatrix} = \frac{-l}{2} \cdot \lambda \cdot \begin{bmatrix} p_x \\ p_y \end{bmatrix} + \begin{bmatrix} x_c \\ y_c \end{bmatrix} \tag{8}$$

A more in-depth analysis is required to obtain the aperture misalignment δ (see Fig. 6.b), where the corners of the tilted aperture (red square in Fig. 6.b) are denoted as $\mathbf{Q_1}$, $\mathbf{Q_2}$, $\mathbf{Q_3}$ and $\mathbf{Q_4}$ (9 - 12).

$$\mathbf{Q_1} = \left(x_r + \frac{l}{\sqrt{2}} \cdot cos(45+\delta), y_r + \frac{l}{\sqrt{2}} \cdot sin(45+\delta)\right) \tag{9}$$

$$\mathbf{Q_2} = \left(x_r + \frac{l}{\sqrt{2}} \cdot cos(135+\delta), y_r + \frac{l}{\sqrt{2}} \cdot sin(135+\delta)\right) \tag{10}$$

$$\mathbf{Q_3} = \left(x_r + \frac{l}{\sqrt{2}} \cdot cos(225+\delta), y_r + \frac{l}{\sqrt{2}} \cdot sin(225+\delta)\right) \tag{11}$$

$$\mathbf{Q_4} = \left(x_r + \frac{l}{\sqrt{2}} \cdot cos(315+\delta), y_r + \frac{l}{\sqrt{2}} \cdot sin(315+\delta)\right) \tag{12}$$

These equations can be simplified into (13 - 16), by taking into account some straightforward trigonometric considerations and assuming small values of δ, so $\sin(\delta) \approx \delta$ and $\cos(\delta) \approx 1$.

$$\mathbf{Q_1} = (x_1, y_1) = \left(x_r + \frac{l}{2} \cdot (1-\delta), y_r + \frac{l}{2} \cdot (1+\delta)\right) \tag{13}$$

$$\mathbf{Q_2} = (x_2, y_2) = \left(x_r + \frac{l}{2} \cdot (-1-\delta), y_r + \frac{l}{2} \cdot (1-\delta)\right) \tag{14}$$

$$\mathbf{Q_3} = (x_3, y_3) = \left(x_r + \frac{l}{2} \cdot (-1+\delta), y_r + \frac{l}{2} \cdot (-1-\delta)\right) \tag{15}$$

$$\mathbf{Q_4} = (x_4, y_4) = \left(x_r + \frac{l}{2} \cdot (1+\delta), y_r + \frac{l}{2} \cdot (-1+\delta)\right) \tag{16}$$

As can be observed in Fig. 6.b), the intersection points of the X axis with the line from $\mathbf{Q_4}$ to $\mathbf{Q_1}$ and with the line from $\mathbf{Q_3}$ to $\mathbf{Q_2}$ are denoted as x_{41} and x_{32}, respectively. Similarly, the intersection points of the Y axis with the line from $\mathbf{Q_2}$ to $\mathbf{Q_1}$ and with the line from $\mathbf{Q_3}$ to $\mathbf{Q_4}$ are denoted as y_{21} and y_{34}, respectively.

$$x_{41} = \frac{x_1 - x_4}{y_1 - y_4} \cdot (-y_1) + x_1 = \\ -\delta \cdot \left(-y_r - \frac{l}{2} \cdot (1+\delta)\right) + \left(x_r + \frac{l}{2} \cdot (1-\delta)\right) \tag{17}$$

$$x_{32} = \frac{x_2 - x_3}{y_2 - y_3} \cdot (-y_2) + x_2 = \\ -\delta \cdot \left(-y_r - \frac{l}{2} \cdot (1-\delta)\right) + \left(x_r - \frac{l}{2} \cdot (1+\delta)\right) \tag{18}$$

$$y_{21} = \frac{y_1 - y_2}{x_1 - x_2} \cdot (-x_2) + y_2 = \\ \delta \cdot \left(-x_r + \frac{l}{2} \cdot (1+\delta)\right) + \left(y_r + \frac{l}{2} \cdot (1-\delta)\right) \tag{19}$$

$$y_{34} = \frac{y_4 - y_3}{x_4 - x_3} \cdot (-x_3) + y_3 = \\ \delta \cdot \left(-x_r + \frac{l}{2} \cdot (1-\delta)\right) + \left(y_r - \frac{l}{2} \cdot (1+\delta)\right) \tag{20}$$

Finally, the centre $(x_{r,\delta},\ y_{r,\delta})$ of the illuminated square area when only the misalignment of the aperture is taken into account is obtained according to (21) and (22).

$$x_{r,\delta} = \frac{x_{41} + x_{32}}{2} = \delta \cdot y_r + x_r \tag{21}$$

$$y_{r,\delta} = \frac{y_{21} + y_{34}}{2} = -\delta \cdot x_r + y_r \tag{22}$$

Therefore, a final expression can be achieved by rewriting (8) and adding the effects of δ. Then, the central incident point considering all the parameters $\left(\begin{bmatrix} x_{r,\lambda,c,\delta} \\ y_{r,\lambda,c,\delta} \end{bmatrix}\right)$ is obtained according to (23).

$$\begin{bmatrix} x_{r,\lambda,c,\delta} \\ y_{r,\lambda,c,\delta} \end{bmatrix} = \frac{-l}{2} \cdot \lambda \cdot \begin{bmatrix} p_x + \delta \cdot p_y \\ -\delta \cdot p_x + p_y \end{bmatrix} + \begin{bmatrix} x_c \\ y_c \end{bmatrix} \tag{23}$$

B. Positioning Algorithm

For the ideal case, the aforementioned equations can be simplified as (24) and (25), whether $l = 2.75\,\text{mm}$, $\delta = 0$, $\lambda = 1$, and $(x_c, y_c) = (0, 0)$.

$$x_r = -\frac{11}{8} \cdot p_x\,\text{mm} \tag{24}$$

$$y_r = -\frac{11}{8} \cdot p_y\,\text{mm} \tag{25}$$

The ratios p_x and p_y are obtained by combining the maximum values of the correlated signals $s_i[n]$, $t_i[n]$ and $r_i[n]$ [24], as presented in (26) and (27).

Note that since $s_i[n]$, $t_i[n]$ and $r_i[n]$ are the outputs of correlation processes, their maximum peaks are a representation of the energy received from each transmitter i for the three acquired signals V_{sum}, V_{bt} and V_{lr}, respectively.

$$p_x = \frac{max(r_i[n])}{max(s_i[n])} \tag{26}$$

$$p_y = \frac{max(t_i[n])}{max(s_i[n])} \tag{27}$$

After estimating the i^{th} positions of the central incident ray for each transmitter $(x_{r,i}, y_{r,i})$ in the QADA photodiode, the algorithm detects the rotation β of the receiver. Since the transmitters are arranged in a square geometry, the image points on the QADA receiver should present the same shape. If the receiver is rotated a certain angle β around the Z axis, the image points will be also rotated β degrees around the Z axis. In this way, trigonometric equations are used to estimate the current rotation angle β by using the rotated image points $(x_{r,i}, y_{r,i})$ [17]. Afterwards, the image points $(x_{r,i}, y_{r,i})$ are rotated $-\beta$ degrees to undo the rotation of the receiver to find the non-rotated image points $(x'_{r,i}, y'_{r,i})$. This step is crucial since the following positioning algorithm does not operate properly whether the receiver is rotated. Once the central impact points are rotated, the positioning algorithm continues

to the final estimation of the receiver's position $(x,\ y)$ in the proposed scenario, by means of a Least Squares Estimator (LSE) as $(x, y) = (\mathbf{A}^T \cdot \mathbf{A})^{-1} \cdot \mathbf{A}^T \cdot \mathbf{b}$, where (28):

$$\mathbf{A} = \begin{bmatrix} -y'_{r,1} & x'_{r,1} \\ -y'_{r,2} & x'_{r,2} \\ -y'_{r,3} & x'_{r,3} \\ -y'_{r,4} & x'_{r,4} \end{bmatrix} \quad \mathbf{b} = \begin{bmatrix} y_{t,1} \cdot x'_{r,1} - x_{t,1} \cdot y'_{r,1} \\ y_{t,2} \cdot x'_{r,2} - x_{t,2} \cdot y'_{r,2} \\ y_{t,3} \cdot x'_{r,3} - x_{t,3} \cdot y'_{r,3} \\ y_{t,4} \cdot x'_{r,4} - x_{t,4} \cdot y'_{r,4} \end{bmatrix} \tag{28}$$

Note that $(x_{t,i}, y_{t,i}, z_{t,i})$ are the transmitters' position. After estimating the receiver's position $(x,\ y)$, the coordinate z is obtained by taking into account the trigonometric considerations that involve the incident angle ψ_i and the distance d_i between the estimated receiver's position and the projection of each transmitter on the plane where the receiver is placed, as $z_i = z_{t,i} - \frac{d_i}{tan(\psi_i)}$. The incident angle ψ_i is obtained from the aperture height h_{ap} and the impact point at the receiver $(x_{r,i}, y_{r,i})$ [24]. More detailed information about it can be found in the pseudocode Algorithm 1 presented below.

Algorithm 1 Positioning algorithm

for $i = 1 : 4$ **do**
    LED i emits code c_i
end for
QADA receiver detects codes c_i simultaneously
$[V_{sum},\ V_{bt},\ V_{lr}]$ = QADAGenerateSignals (c_i)
for $i = 1 : 4$ **do**
    $[s_i[n], t_i[n], r_i[n]]$ = Correlation $([V_{sum},\ V_{bt},\ V_{lr}],\ c_i)$
    $[p_{x,i}, p_{y,i}] = \frac{[max(r[n]_i), max(t[n]_i)]}{max(s[n]_i)}$
    $[x_{r,i}, y_{r,i}] = -\frac{11}{8}[p_{x,i}, p_{y,i}]$ ▷ Central Impact Point
    β = EstimateQADARotation$(x_{r,i}, y_{r,i})$
    $[x'_{r,i}, y'_{r,i}]$ = RotationCentralImpactPoint$(x_{r,i}, y_{r,i}, -\beta)$
end for
$[x, y]$ = ReceiverPositionEstimation(x'_r, y'_r) ▷ Eq.(28)
$z = z_t - \frac{d}{tan(\psi)}$

IV. Transmission Encoding Techniques

Since the transmission of the different sequences is simultaneous for all the emitters, each LED i transmits its own BPSK modulated sequence c_i. Concerning the modulation process, three main parameters have to be defined: the type of carrier, the number M of samples per carrier period, and the number N_c of carrier periods representing every bit. The modulated signal emitted by the i^{th} emitter is given by (29):

$$m_i[n] = c_i \left[\frac{n}{N_c \cdot M} \right] \cdot s[n] \quad for \quad n = 0, 1, ... N_c \cdot M \cdot L - 1 \tag{29}$$

Where $m_i[n]$ is the modulated signal in the discrete time domain n; $c_i[n]$ is still the binary sequence used to encode the emission; L is the length of this sequence; and $s[n] = sin(2 \cdot \pi \cdot f_c \cdot n \cdot T_s)$ is the modulation carrier, with a symbol formed by N_c periods of the carrier, and $M = f_s/f_c$ samples per period. Note that f_c is the carrier frequency, whereas $f_s = 1/T_s$ is the sampling frequency.

Although all the transmitted codes are merged at the receiver, the use of a different code per beacon (see Fig. 7), with suitable cross-correlation properties, allows the later processing algorithm to discriminate the signals coming from each emitter and obtain the corresponding AoA. To remove the LED's flickering while transmitting the codes c_i, a much higher carrier frequency than 200 Hz has been selected. In particular, the carrier frequency of the BPSK modulation is $f_c = 25\,\text{kHz}$, whereas the sampling frequency is $f_s = 250\,\text{kHz}$ (i.e. $M = 10$).

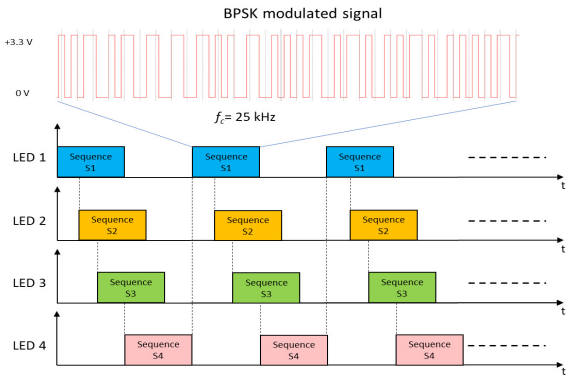

Fig. 7. Global view of the transmission scheme for the codes c_i.

Another aspect to consider is that the reception of the sequences can be degraded by the MAI effect, as a result from the simultaneous transmission and reception, as well as due to limitations in the channel or the transmitters' bandwidth, interferences in the correlation of signals, etc. Furthermore, not all sequences have the same correlation scheme (see Fig. 8), hence they behave differently against the MAI effect. Therefore, it is important to analyse those sequences that may minimize the MAI effect at reception, so that the final estimation of the receiver's position is improved.

In order to enhance the receiver's position estimation, it is essential to have a suitable correlation function. The Sidelobe-to-Mainlobe Ratio (SMR) is a parameter commonly related to correlation functions (see Fig. 8) that is of great interest in the design of a sequence. A high value of SMR indicates that the main lobe may be confused with a sidelobe, thus resulting in inaccurate results. The behaviour of pseudo-random sequences, such as Kasami codes, as well as complementary pairs of sequences, such as LS sequences, is studied from the point of view of the SMR parameter, in order to determine their performance in the proposed system.

LS sequences have, in addition to low SMR, another relevant feature to consider: the Interference Free Window (IFW), which is a zone where the auto correlations and cross correlations are null. In particular, LS sequences present a zero-correlation zone around the origin (see Fig. 8.a). On the other hand, Kasami sequences have higher SMR than LS sequences. However, if not only the samples within the IFW are considered, then LS sequences present a higher SMR (see Fig. 8.b). In order to accurately determine the IFW of the sequence in a transmission, it is crucial to have a pseudo-synchronization between emitters and receivers.

The length of the IFW depends on the design of the sequence; for example, the 1151-bit LS sequence is based on two sets of 512 bits with 127 zeros in between [25], so the IFW is 127 long. There is a trade-off between maximizing the IFW and having an extremely long sequence. A consistent localization of the IFW is key to clearly detect the mainlobe of the correlation signal and, hence, have a low SMR. Note that there is a significant sidelobe at both ends of the IFW.

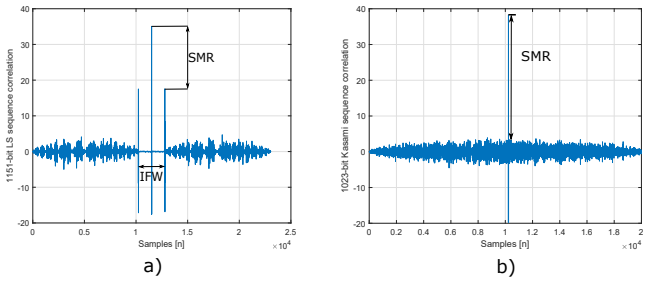

Fig. 8. Example of auto-correlation functions: a) 1151-bit LS and b) 1023-bit Kasami.

V. Simulated Results

Hereinafter, Kasami and LS sequences are used in the estimation of the receiver's position. In simulations, the volume under analysis is $2 \times 2 \times 3.4\,\mathrm{m}^3$ (a distance of $3.4\,\mathrm{m}$ between transmitters and the plane where the receiver moves), the number of measurements per analysed point is 50, and the SNR is $10\,\mathrm{dB}$. This value has been selected since in the experimental tests it has been checked that typical values of SNR in the environment are around $10\,\mathrm{dB}$. The transmitters' positions were already presented in Table I.

A general analysis is detailed in Fig. 9, where the Cumulative Distribution Function (CDF) of the absolute position error for the three coordinates is presented for Kasami and LS sequences, according to their lengths L. The 1023-bit Kasami code results in the worst sequence to use, obtaining absolute errors for coordinates x and y of almost $10\,\mathrm{cm}$, whereas coordinate z has errors of $40\,\mathrm{cm}$ in the 90% of cases. On the other hand, it can be observed how the 1151-bit LS sequences achieve the best performance, where errors below $3\,\mathrm{cm}$ are achieved in the 90% of cases for coordinates x and y.

It is worth mentioning that a sequence shifting or displacement can improve the cross-correlation properties of the codes at the receiver, as the time of arrival is considered to be the same for all emissions. This sequence shifting actually implies a displacement of a certain number of samples in the emission of a LED i with regard to the previous one, thus avoiding a fully simultaneous transmission by all the transducers.

In order to clearly select the most suitable displacement for the 1151-bit LS sequence, the SMR of the different correlated signals has been analysed with respect to the number of displaced samples. It has been confirmed that, whether the selected displacement is 10 samples or higher, the SMR remains constant at SMR $= 0.5$.

In addition to the previous analysis, in Fig. 10 an 1151-bit LS sequence with displacements of 3, 4, 10, 12 and 15 samples

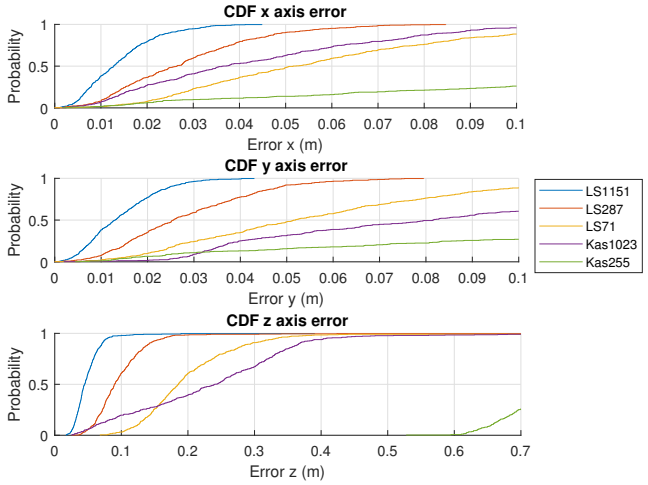

Fig. 9. CDF for the absolute error in the estimation of the receiver's position in coordiantes x, y and z for different types of sequences.

is considered to estimate the receiver's position. Fig. 10.a) plots the global CDF, whereas Fig. 10.b) is a particular zoom. It can be observed that at the 90% of the CDF the obtained absolute error values are $1.8 - 2\,\mathrm{cm}$, achieving the best performance when the sequence is shifted 10 samples. Therefore, hereinafter a 1151-bit LS sequence with a displacement of 10 samples is considered.

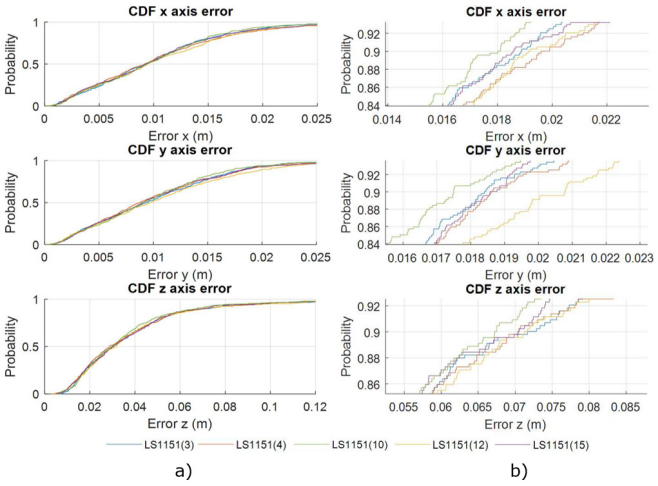

Fig. 10. CDF for the absolute error in the estimation of the receiver's position in coordinates x, y and z using a 1151-bit LS sequence with a displacement of 3, 4, 10, 12 and 15 samples.

A similar analysis has been performed for the Kasami sequences, finding five samples (half a modulation symbol) to be a suitable trade-off between minimizing the positioning error and having a simultaneous transmission [17] [24].

On the other hand, in [17] it is indicated that the lowest and the highest errors in the estimation of the receiver's position, whether there is a rotation in the Z axis, occurs when the receiver is rotated 5° and 45° for the first quadrant, respectively. The study of a quadrant in the proposed scenario can be extended to the rest of the grid due to the symmetry existing in the transmitters' arrangement. Therefore, six points have

been analysed in the proposed scenario when the transmitters are located at $z_{t,i} = \{2\,\mathrm{m}, 3.4\,\mathrm{m}\}$ and for both rotational angles β. Figs. 11 and 12 depict the position estimates, using a 1151-bit LS sequence with a displacement of 10 samples and a 1023-bit Kasami with a displacement of 5 samples, respectively. The black crosses represent the projection of the LED's coordinates; the red crosses are the ground-truth of the measurements; and the coloured point clouds are the estimated receiver's position. An error ellipsoid is also plotted with a 95% of confidence for every test point.

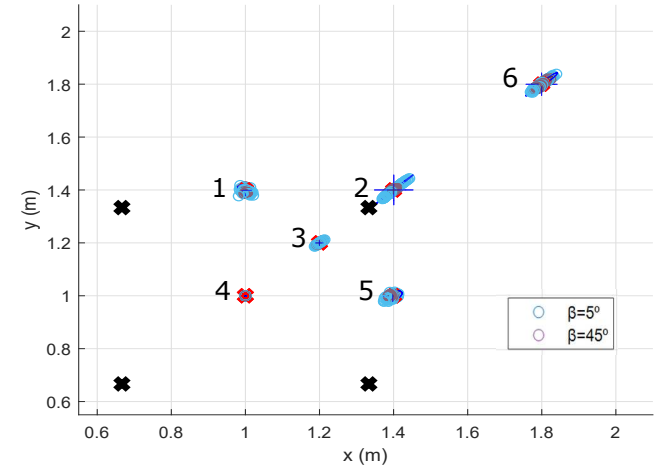

(a)

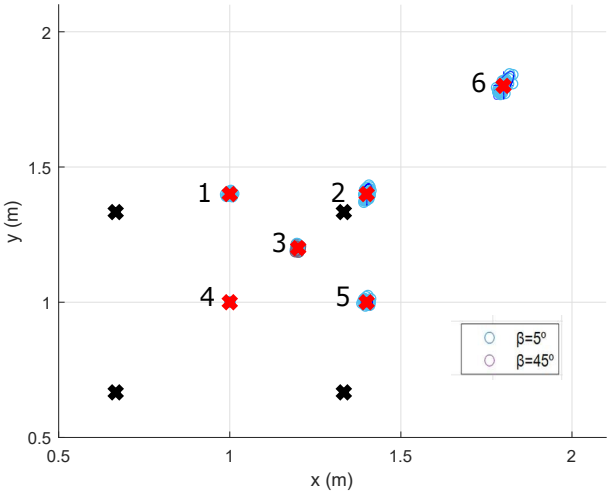

(b)

Fig. 11. Simulated position estimates for $\beta = 5°, 45°$ with the transmission of a 1151-bit LS sequence with a displacement of 10 samples for: a) $z_t = 2\,\mathrm{m}$; and b) $z_t = 3.4\,\mathrm{m}$.

It can be observed that the centres of the error ellipsoids in the estimated points in Fig. 12.a) do not match the ground-truth in any of the proposed polar angles. In fact, the absolute errors in the corners of the grid are noticeable compared to those obtained in the centre of the grid (see point 6 versus point 4). On the other hand, comparing the implementation of Kasami and LS sequences in Figs. 11 and 12, respectively, the absolute error is highly decreased when a LS sequence is used and, thus, the MAI effect is nearly discarded. This

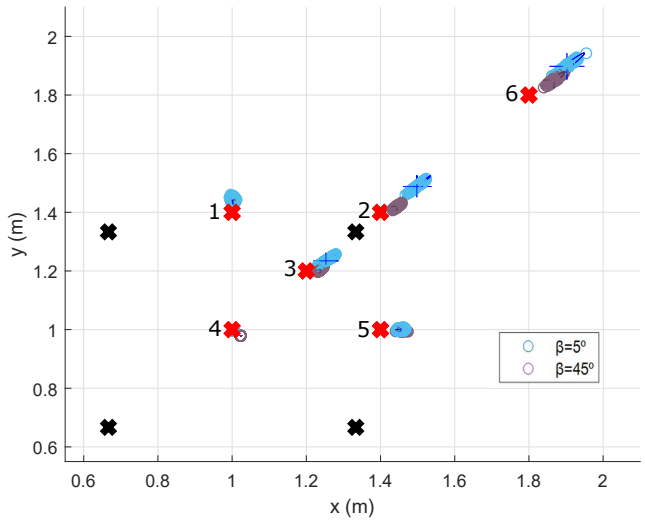

(a)

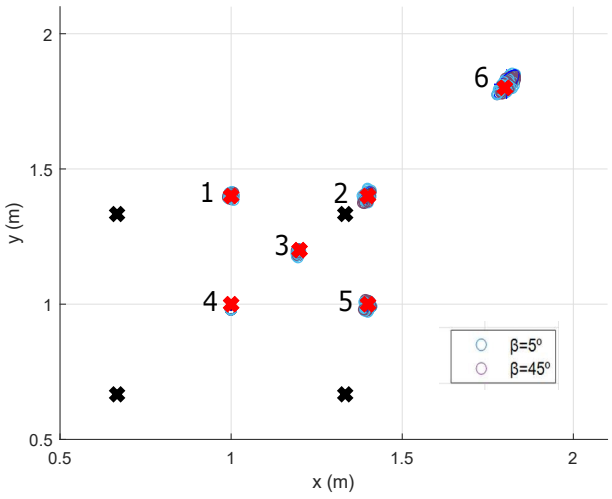

(b)

Fig. 12. Simulated position estimates for $\beta = 5°, 45°$ with the transmission of a 1023-bit Kasami sequence with a displacement of 5 samples for: a) $z_t = 2\,\mathrm{m}$ and b) $z_t = 3.4\,\mathrm{m}$.

improvement has been achieved through the use of a robust sequence against MAI, such as the 1151-bit LS sequence with a displacement of 10 samples.

The values of the average absolute error and the standard deviation for the six points analysed for every polar angle and every sequence are further detailed in Tables II to V and in the box diagram presented in Fig. 13. It is noticeable that, although the standard deviation remains very similar in both cases, whether the LS sequence is used in the transmission, the average absolute errors in the estimation of the different coordinates are highly decreased.

VI. Receiver Calibration

Similarly to the analysis plotted in Fig. 11.b) with $z_t = 3.4$m, points 1, 2 and 4 have been experimentally analysed in Fig. 14 for the polar angles $\beta = \{0°, 120°, 210°, 300°\}$ using a 1151-bit LS sequence with a displacement of 10 samples.

TABLE II
SIMULATED AVERAGE ABSOLUTE ERROR AND STANDARD DEVIATION FOR THE ANALYSED POINTS WITH A 1023-BIT KASAMI SEQUENCE FOR $z_t = 2\,\text{m}$.

		Average absolute error (cm)			**Standard deviation (cm)**		
	Polar angle β	*X axis*	*Y axis*	*Z axis*	*X axis*	*Y axis*	*Z axis*
Point 1	5º	0,27	4,55	14,92	0,22	0,49	1,44
	45º	0,40	4,26	18,42	0,23	0,64	2,37
Point 2	5º	9,63	8,66	39,20	1,37	1,30	11,25
	45º	4,50	2,04	5,25	0,58	0,52	3,96
Point 3	5º	5,52	3,68	16,62	1,32	1,11	5,82
	45º	3,69	0,35	18,61	0,34	0,25	3,84
Point 4	5º	0,40	0,38	14,13	0,02	0,02	1,73
	45º	2,27	2,09	14,63	0,02	0,02	1,73
Point 5	5º	5,45	0,23	15,34	0,54	0,18	1,58
	45º	5,75	0,31	20,17	0,58	0,20	2,28
Point 6	5º	10,59	10,07	25,58	1,58	1,58	4,26
	45º	6,86	5,26	14,46	1,00	0,94	2,77
Total		4,61	3,49	18,11	0,65	0,60	3,59

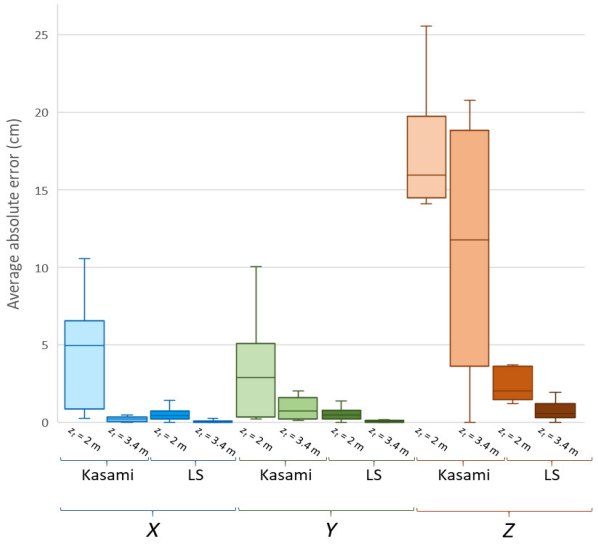

Fig. 13. Average absolute errors for the analysed points in simulation with a 1023-bit Kasami and 1151-bit LS sequence for $z_t = 2\,\text{m}$ and $z_t = 3.4\,\text{m}$ (X error in blue, Y error in green and Z error in brown).

TABLE III
SIMULATED AVERAGE ABSOLUTE ERROR AND STANDARD DEVIATION FOR THE ANALYSED POINTS WITH A 1023-BIT KASAMI SEQUENCE FOR $z_t = 3.4\,\text{m}$.

		Average absolute error (cm)			**Standard deviation (cm)**		
	Polar angle β	*X axis*	*Y axis*	*Z axis*	*X axis*	*Y axis*	*Z axis*
Point 1	5º	0,01	0,16	20,39	0,42	0,66	5,34
	45º	0,01	0,21	20,78	0,39	0,51	4,40
Point 2	5º	0,21	0,12	14,24	0,59	1,18	12,52
	45º	0,20	0,20	17,62	0,51	1,04	11,36
Point 3	5º	0,33	0,72	18,96	0,28	0,60	6,77
	45º	0,36	0,79	18,58	0,25	0,61	6,65
Point 4	5º	0,07	2,01	9,31	0,05	0,06	4,65
	45º	0,07	2,01	8,13	0,05	0,06	3,95
Point 5	5º	0,25	0,89	0,12	0,54	0,87	4,42
	45º	0,29	0,56	0,03	0,49	1,01	3,82
Point 6	5º	0,50	1,30	3,18	1,28	1,89	6,98
	45º	1,03	1,69	4,97	1,16	1,68	5,90
Total		0,28	0,89	11,36	0,50	0,85	6,40

TABLE IV
SIMULATED AVERAGE ABSOLUTE ERROR AND STANDARD DEVIATION FOR THE ANALYSED POINTS WITH A 1151-BIT LS SEQUENCE FOR $z_t = 2\,\text{m}$.

		Average absolute error (cm)			**Standard deviation (cm)**		
	Polar angle β	*X axis*	*Y axis*	*Z axis*	*X axis*	*Y axis*	*Z axis*
Point 1	5º	0,56	0,71	1,79	0,53	0,51	1,25
	45º	0,22	0,52	1,88	0,16	0,37	1,41
Point 2	5º	1,58	1,73	32,00	1,05	1,12	43,00
	45º	0,44	0,41	13,06	0,33	0,31	18,27
Point 3	5º	0,41	0,37	3,27	0,35	0,33	2,63
	45º	0,29	0,28	2,33	0,20	0,19	1,62
Point 4	5º	0,01	0,01	1,40	0,01	0,01	1,02
	45º	0,01	0,01	1,23	0,01	0,01	1,02
Point 5	5º	0,64	0,60	1,58	0,50	0,55	1,27
	45º	0,39	0,21	1,42	0,30	0,16	1,09
Point 6	5º	1,44	1,39	3,73	0,90	0,86	2,56
	45º	0,79	0,81	2,20	0,55	0,54	1,53
Total		0,57	0,59	5,49	0,41	0,41	6,39

TABLE V
SIMULATED AVERAGE ABSOLUTE ERROR AND STANDARD DEVIATION FOR THE ANALYSED POINTS WITH A 1151-BIT LS SEQUENCE FOR $z_t = 3.4\,\text{m}$.

		Average absolute error (cm)			**Standard deviation (cm)**		
	Polar angle β	*X axis*	*Y axis*	*Z axis*	*X axis*	*Y axis*	*Z axis*
Point 1	5º	0,09	0,11	0,96	0,36	0,52	4,24
	45º	0,11	0,01	0,02	0,41	0,51	4,19
Point 2	5º	0,03	0,12	1,30	0,61	1,01	15,16
	45º	0,02	0,06	0,39	0,69	1,17	12,47
Point 3	5º	0,11	0,06	1,94	0,28	0,62	4,50
	45º	0,07	0,07	0,50	0,31	0,66	4,79
Point 4	5º	0,01	0,01	0,65	0,01	0,01	3,47
	45º	0,01	0,00	0,52	0,01	0,01	3,53
Point 5	5º	0,01	0,09	0,15	0,45	0,67	3,73
	45º	0,03	0,07	0,28	0,50	0,62	4,23
Point 6	5º	0,12	0,16	0,88	1,22	2,13	7,03
	45º	0,25	0,47	1,35	1,14	2,05	7,01
Total		0,07	0,10	0,77	0,50	0,83	6,20

These points have been selected due to their particular location: point 1 is between the projections of two transmitters in the side of the test area (grid) considered; point 2 is below a transmitter in the corner of the grid; and point 4 is near of the centre of the grid. In that way, they are placed in representative points of one of the octants of the system. The following analysis and considerations can be extended to the rest of the octants of the grid, due to the symmetries existing in the transmitters' arrangement. In the same way, the polar angles β are selected to verify that very different orientations of the sensor at each point behave similarly.

While performing the experimental tests, the importance of a suitable previous calibration emerged (see Fig. 14). Before calibration, the global average absolute error obtained for coordinates x and y is 8.5 cm and the standard deviation is 1.6 cm. Coordinate z achieves an average absolute error of 1 m and a standard deviation of 30 cm. These errors are mainly coming from undesired misalignments in the experimental

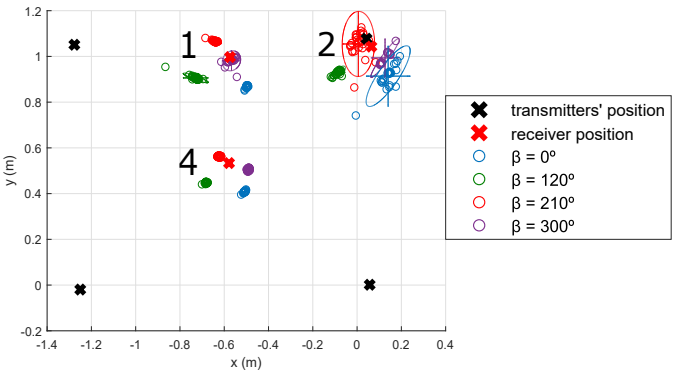

Fig. 14. Experimental position estimates for $\beta = \{0°, 120°, 210°, 300°\}$ with a 1151-bit LS sequence and a displacement of 10 samples without calibration.

setup, related to the optical centre (x_c, y_c), the height h_{ap} at which the aperture is located, the aperture misalignment δ and the length l of the aperture (see Fig. 6).

Therefore, it is necessary to calibrate the receiver in order to improve the obtained results by minimizing undesired misalignments. One of the most commonly used algorithms in camera calibration is the Zhang Method [19], where several images are taken typically from a checkerboard. This method is unfeasible in this proposal since we only have 4 image points (the 4 transmitters) against the 49 image points that a checkerboard provides. Besides, this method does not calibrate the aperture misalignment δ, since cameras involve lenses instead of apertures. Therefore, a novel calibration algorithm is proposed here, which combines iterative methods to obtain the optimized parameters in (23), by using experimental data (see the pseudocode 2 presented below).

Firstly, the aperture height h_{ap}, or focal length in the optical system, has been estimated according to (30) (see Fig. 15), where D and d are the distances between pairs of transmitters obtained with the Optitrack system and pairs of image points, respectively [26]; and H is the height at which the transmitters are located. The obtained aperture height is h_{ap} = 2.55 mm.

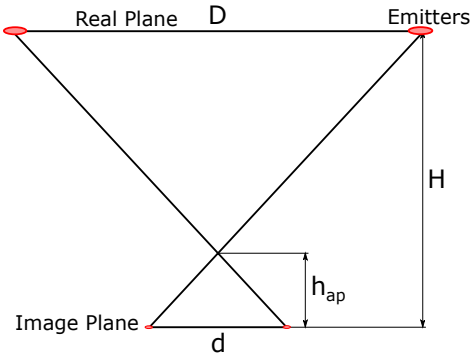

Fig. 15. Calibration of the aperture height h_{ap} using the relation between distances in the real and image worlds.

$$h_{ap} = \frac{H}{\frac{D}{d}+1} \tag{30}$$

Algorithm 2 Calibration algorithm pseudo-code

Phase 1 - Estimation of the aperture height

$h_{ap} = \frac{H}{\frac{D}{d}+1}$

Phase 2 - Estimation of the optical centre (x_c, y_c) using a Branch and Bound algorithm

while $step > tolerance$ **do**
  for $x_c = min_x : step : max_x$ **do**
    for $y_c = min_y : step : max_y$ **do**
      [x,y] = PositioningAlgorithm(x_c, y_c)
      $Grid(x_c, y_c)$ = std(x,y)
    end for
  end for
  [$value_x$, $value_y$] = find(max($Grid$))
  [min_x, min_y] = [$value_x$, $value_y$] - [$step$, $step$]
  [max_x, max_y] = [$value_x$, $value_y$] + [$step$, $step$]
  $step$ = $step$/2
end while

Phase 3 - Estimation of the focal length adjustment λ using a Branch and Bound algorithm

while $step > tolerance$ **do**
  for $h_{ap} = min : step : max$ **do**
    z = PositioningAlgorithm(h_{ap})
    $Grid(h_{ap})$ = std(z)
  end for
  $value$ = find(max($Grid$))
  min = $value$ - $step$
  max = $value$ + $step$
  $step$ = $step$/2
end while

Phase 4 - Estimation of the aperture misalignment δ using LLS

$\delta = pinv(\mathbf{J}) \cdot \begin{bmatrix} \mathbf{r_x} \\ \mathbf{r_y} \end{bmatrix}$

Secondly, the optical centre (x_c, y_c) and the focal length adjustment λ have been determined, by applying a Branch and Bound algorithm that minimizes the experimental positioning error. The optical centre has been estimated by minimizing the 2D standard deviation, whereas the focal length adjustment λ has been determined by minimizing the standard deviation of coordinate z.

The Branch and Bound algorithm recursively splits the search space into smaller spaces while keeping track of minimum and maximum bounds that reduce the search space and neglecting the solutions that are not optimal. In this proposal, the algorithm starts testing all the possible solutions within a search space. Then, it finds the value that minimizes the standard deviation and updates the maximum and minimum bounds as one step forward and backwards from that value. This method is recursively repeated by dividing by half the step at each iteration, until it reaches a certain tolerance.

In particular, in order to estimate the optical centre we have

set (1,1) mm and (−1,−1) mm as the initial maximum and minimum bounds, respectively, and 0.1 mm as the initial step. The algorithm stops when the step is 0.025 mm, therefore, just three iterations are needed. On the other hand, in order to estimate the focal length adjustment, the initial maximum and minimum bounds are 2 and 0.5, respectively, and the step is set at 0.1. In this case, the algorithm stops when the step is 0.05, so that only two iterations are required. The optical centre and the focal length adjustment have been determined at (x_c, y_c) = (0.055, −0.035) mm and $\lambda = 1.25$, respectively. Note that the radius of the QADA sensor is 3.9 mm and a slightly off-centre aperture may imply high errors in the estimation of the receiver's position. Finally, to find the misalignment δ of the aperture, Linear Least Squares (LLS) with the Moore-Penrose Pseudoinverse are applied to minimize the error in the estimation of the image points (23) using the experimental measurements, as well as the ground-truth of the measured points.

The algorithm starts calculating the residuals $\begin{bmatrix} r_x \\ r_y \end{bmatrix}_{P_j,\beta,i}$ by applying (31), where $\begin{bmatrix} \hat{x}_r \\ \hat{y}_r \end{bmatrix}_{P_j,\beta,i}$ is the ideal image point for each transmitter i obtained for each point P_j and rotation β in Fig. 14, and $f(\mathbf{p}_{P_j,\beta,i}, \delta)$ is defined in (32), where $\mathbf{p}_{P_j,\beta,i}$ are the measured values of p_x and p_y for a particular point P_j with $j = \{1, 2, 4\}$ (points selected for calibration) and a rotation angle β for each transmitter i. The ratios p_x and p_y are the measured values from the correlation peaks, as shown in (26) and (27). The length l of the aperture, the focal length adjustment λ and the optical centre (x_c, y_c) are obtained according to the above-mentioned calibration.

$$\begin{bmatrix} r_x \\ r_y \end{bmatrix}_{P_j,\beta,i} = \begin{bmatrix} \hat{x}_r \\ \hat{y}_r \end{bmatrix}_{P_j,\beta,i} - f(\mathbf{p}_{P_j,\beta,i}, \delta) \tag{31}$$

$$f(\mathbf{p}_{P_j,\beta,i}, \delta) = \frac{-l}{2} \cdot \lambda \cdot \begin{bmatrix} p_x + \delta \cdot p_y \\ -\delta \cdot p_x + p_y \end{bmatrix}_{P_j,\beta,i} + \begin{bmatrix} x_c \\ y_c \end{bmatrix} \tag{32}$$

In addition, the Jacobian matrix for a certain transmitter i is defined in (33) for a particular point P with a certain rotation β, according to δ.

$$J_{P_j,\beta,i} = \frac{\partial f(\mathbf{p}_{P_j,\beta,i}, \delta)}{\partial \delta} = \frac{-l}{2} \cdot \lambda \cdot \begin{bmatrix} p_y \\ -p_x \end{bmatrix}_{P_j,\beta,i} \tag{33}$$

After the residuals are obtained for all the points considered, the solution for the misalignment δ is obtained by means of an oversized system and using the pseudoinverse matrix ($pinv$), according to (34). Note that $\mathbf{r_x}$ and $\mathbf{r_y}$ are vectors with a length of 48 each, since the number of experimental points P_j is 3, the number of considered rotation angles β is 4, and the number of transmitters i is also 4. Therefore, the vector $\mathbf{J}$ has a length of 96. The value of the misalignment provided by this method is δ = 0.1 rad.

$$\delta = pinv(\mathbf{J}) \cdot \begin{bmatrix} \mathbf{r_x} \\ \mathbf{r_y} \end{bmatrix} = pinv \left(\begin{bmatrix} \frac{-l}{2} \cdot \lambda \cdot p_{y_{P_1,0°,1}} \\ \frac{-l}{2} \cdot \lambda \cdot p_{y_{P_1,120°,1}} \\ \cdots \\ \frac{-l}{2} \cdot \lambda \cdot p_{y_{P_4,300°,4}} \\ \frac{-l}{2} \cdot \lambda \cdot (-p_{x_{P_1,0°,1}}) \\ \frac{-l}{2} \cdot \lambda \cdot (-p_{x_{P_1,120°,1}}) \\ \cdots \\ \frac{-l}{2} \cdot \lambda \cdot (-p_{x_{P_4,300°,4}}) \end{bmatrix} \right) \cdot \begin{bmatrix} r_{x_1} \\ r_{x_2} \\ \cdots \\ r_{x_{48}} \\ r_{y_1} \\ r_{y_2} \\ \cdots \\ r_{y_{48}} \end{bmatrix} \tag{34}$$

VII. Experimental Results

The experimental tests have been carried out in a room of 2 x 2 m^2 with a height of 3.4 m (see Fig. 16) under normal artificial and natural light conditions. The LED beacons are located in the ceiling of the room, distributed in the four corners of a square with a 1.2m long side. The receiver is located on the floor of the room, thus, the final distance between transmitters and the receiver is longer than 3.4 m. Simulations have already verified that the sequence with a worse behaviour in this proposal is the 1023-bit Kasami sequence; therefore, hereinafter, in the experimental tests only the 1151-bit LS sequences have been considered. The receiver is a QADA receiver QP50-6-18u-TO8 with a radius r = 3.9 mm [27]. A square aperture with a side of 2.75 mm has been placed on top of the sensor at a distance $h_{ap} = 2.6$ mm. A synchronism beacon has been included in the proposed system, so that the emission of the different BPSK modulated sequences c_i is simultaneous for all the beacons b_i, as well as their acquisition in the QADA sensor [28].

The Optitrack system is a high accuracy motion capture system that has been used in the determination of the actual positions (ground-truth) of the transmitters and the different positions where the receiver has been placed [26]. It is considered as a way to determine the real positions of transmitters and receiver, but not as alternative method for comparison. This system presents a much more complex architecture than the proposal described here, since it is based on a set of cameras distributed all over the room that allow to obtain the position of the desired object with an accuracy of 0.1 mm.

On the other hand, and similarly to the analysis performed in Fig. 14, points 1, 2 and 4 have been experimentally analysed in Fig. 17 for the polar angles $\beta = \{0°, 120°, 210°, 300°\}$. The average absolute error, the median absolute error and the standard deviation for the three analysed points and the corresponding polar angles $\beta = \{0°, 120°, 210°, 300°\}$ are further detailed in Table VI. After 50 measurements performed at each point, the obtained results for coordinates x, y and z are 3.50 cm, 7.34 cm and 23.32 cm for the total average absolute error, and 1.42 cm, 3.63 cm and 33.60 cm for the standard deviation.

For clarity's sake, a CDF of the absolute errors in the estimation of the receiver's position is presented in Fig. 18. Points 1 and 2, which are located near the corners, present higher errors than the point 4, near the centre of the grid. The results obtained in Figs. 14, 17, and 18 show the importance of an accurate calibration, since the global positioning error has

TABLE VI
EXPERIMENTAL AVERAGE ABSOLUTE ERROR, MEDIAN ABSOLUTE ERROR AND STANDARD DEVIATION FOR THE ANALYSED POINTS WITH A 1151-BIT LS SEQUENCE.

		Average absolute error			**Median absolute error**			**Standard deviation**		
	Polar angle	*X (cm)*	*Y (cm)*	*Z (cm)*	*X (cm)*	*Y (cm)*	*Z (cm)*	*X (cm)*	*Y (cm)*	*Z (cm)*
Point 1	0º	0,47	10,63	52,97	0,47	10,62	52,36	0,31	0,30	4,73
	120º	4,92	3,68	8,01	4,85	3,71	31,65	0,44	0,27	132,14
	240º	0,98	3,05	1,90	1,13	3,15	4,26	0,49	0,41	14,35
	300º	2,87	7,90	0,95	2,88	7,89	2,31	0,43	0,42	10,62
Point 2	0º	2,62	11,82	117,64	2,65	11,74	118,51	0,40	0,48	2,92
	120º	10,57	3,64	12,74	10,27	3,73	17,11	2,04	0,64	13,66
	240º	1,02	6,09	4,76	1,22	1,38	3,15	1,71	25,60	24,78
	300º	4,52	7,41	3,87	4,37	7,13	1,38	1,52	1,25	34,49
Point 3	0º	0,72	11,21	1,75	0,91	9,81	1,41	3,23	4,64	26,33
	120º	10,72	6,53	2,34	10,34	6,01	4,76	1,30	1,09	15,94
	240º	2,19	5,53	14,41	2,27	4,91	5,41	2,89	5,41	88,79
	300º	0,37	10,58	58,47	1,00	12,61	73,27	2,24	3,04	34,39
Total		3,50	7,34	23,32	3,53	6,89	26,30	1,42	3,63	33,60

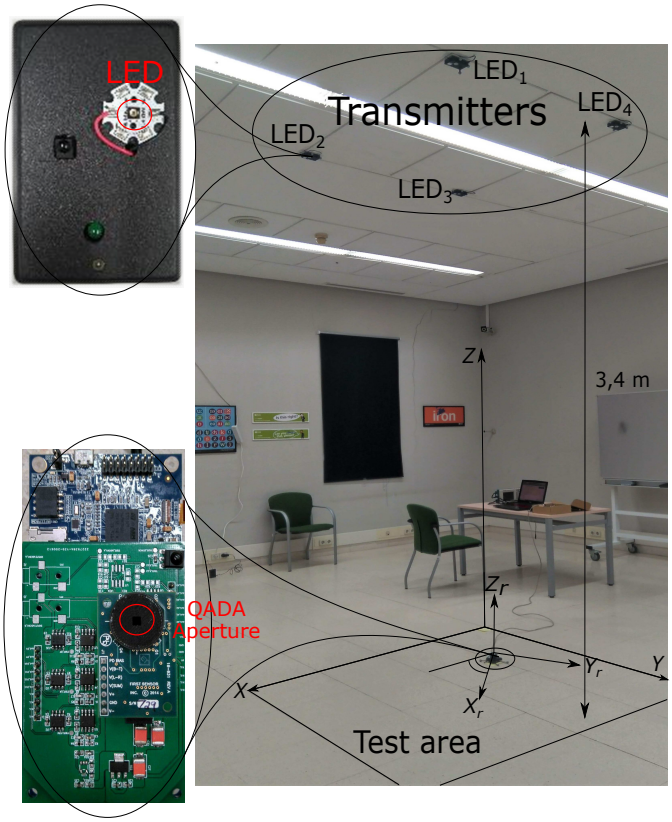

Fig. 16. Experimental setup in the proposed scenario.

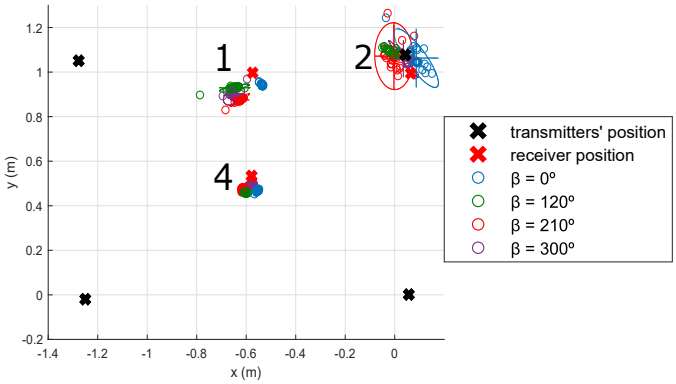

Fig. 17. Experimental position estimates for $\beta = \{0°, 120°, 210°, 300°\}$ with a 1151-bit LS sequence and a displacement of 10 samples.

decreased more than 5 cm for coordinate x, 1 cm for coordinate y and 80 cm for coordinate z.

VIII. CONCLUSIONS

This work has presented a 3D infrared indoor positioning system, based on four LEDs and a quadrant photodiode as a receiver. The proposal is based on applying encoding techniques to the emitters, which emit simultaneously and are discriminated at the receiver. Different encoding binary sequences have been analysed with the aim of minimizing the MAI effect that is detected in real measurements. In particular, a 1023-bit Kasami sequence and a 1151-bit LS sequence have been compared by simulations in a scenario with a size of $2 \times 2\,\mathrm{m}^2$, achieving average absolute positioning errors at a height of $3.4\,\mathrm{m}$ of $0.07\,\mathrm{cm}$ and $0.28\,\mathrm{cm}$; $0.10\,\mathrm{cm}$ and $0.89\,\mathrm{cm}$; and $0.75\,\mathrm{cm}$ and $11.36\,\mathrm{cm}$ for the LS and the Kasami sequences in the coordinates x, y and z, respectively. The standard deviations are similar for both sequences, achieving values of $0.50\,\mathrm{cm}$ and $0.85\,\mathrm{cm}$ in XY plane and $6.4\,\mathrm{cm}$ and $6.2\,\mathrm{cm}$ in coordinate z for the LS and the Kasami sequences, respectively.

A linearization of the positioning algorithm has been key to improve the system performance as well as to simplify the involved algorithms. In addition, a novel calibration algorithm has been defined and applied to the proposal, by combining trigonometric considerations for the aperture height, a Branch and Bound algorithm for the optical centre, and a Linear Least Squares algorithm for the aperture misalignment. The experimental tests achieved average absolute errors and standard deviations of $3.50\,\mathrm{cm}$, $7.34\,\mathrm{cm}$ and $23.32\,\mathrm{cm}$; and

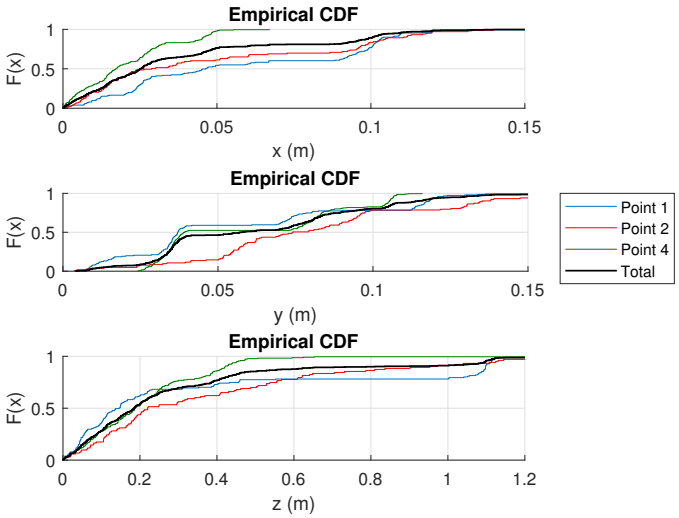

Fig. 18. CDF of the absolute errors of every experimental point for $\beta = \{0°, 120°, 210°, 300°\}$.

1.42 cm, 3.63 cm and 33.60 cm in the coordinates x, y and z, respectively.

REFERENCES

[1] J. Ureña, Á. Hernández, J. J. García, J. M. Villadangos, M. C. Pérez, D. Gualda, F. J. Álvarez, and T. Aguilera, "Acoustic Local Positioning with Encoded Emission Beacons," *Proceedings of the IEEE*, vol. 106, no. 6, pp. 1042–1062, 2018.

[2] C. Wang, L. Wang, X. Chi, S. Liu, W. Shi, and J. Deng, "The research of indoor positioning based on visible light communication," *China Communications*, vol. 12, pp. 85–92, August 2015.

[3] T. Q. Wang, Y. A. Sekercioglu, A. Neild, and J. Armstrong, "Position accuracy of time-of-arrival based ranging using visible light with application in indoor localization systems," *Journal of Lightwave Technology*, vol. 31, no. 20, pp. 3302–3308, 2013.

[4] F. Alam, M. T. Chew, T. Wenge, and G. S. Gupta, "An accurate visible light positioning system using regenerated fingerprint database based on calibrated propagation model," *IEEE Transactions on Instrumentation and Measurement*, vol. 68, pp. 2714–2723, Aug 2019.

[5] G. Z. G. Simon and G. Vakulya, "Lookup: Robust and accurate indoor localization using visible light communication," *IEEE Transactions on Instrumentation and Measurement*, pp. 2337–2348, 2017.

[6] S. Cincotta, C. He, A. Neild, and J. Armstrong, "QADA-PLUS: A Novel Two-Stage Receiver for Visible Light Positioning," *IPIN 2018 - 9th International Conference on Indoor Positioning and Indoor Navigation*, no. September, pp. 24–27, 2018.

[7] P. H. P. H. Pathak, X. Feng and P. Mohapatra, "Visible light communication, networking, and sensing: A survey, potential and challenges," *IEEE Communications Surveys & Tutorials*, pp. 2047–2077, 2015.

[8] J. M. Menéndez and H. Steendam, "Influence of the aperture-based receiver orientation on rss-based vlp performance," in *2017 International Conference on Indoor Positioning and Indoor Navigation (IPIN)*, pp. 1–7, 2017.

[9] C. He, S. Cincotta, M. M. A. Mohammed, and J. Armstrong, "Angular diversity aperture (ada) receivers for indoor multiple-input multiple-output (mimo) visible light communications (vlc)," *IEEE Access*, vol. 7, pp. 145282–145301, 2019.

[10] P. Nabavi and M. Yuksel, "Comprehensive design and prototype of vlc receivers with large detection areas," *Journal of Lightwave Technology*, pp. 1–1, 2020.

[11] Y. S. Eroglu, Y. Yapici, and I. Guvenc, "Impact of Random Receiver Orientation on Visible Light Communications Channel," *IEEE Transactions on Communications*, vol. 67, no. 2, pp. 1313–1325, 2019.

[12] M. Ijaz, Z. Ghassemlooy, S. Ansari, O. Adebanjo, H. Le Minh, S. Rajbhandari, and A. Gholami, "Experimental investigation of the performance of different modulation techniques under controlled fso turbulence channel," in *2010 5th International Symposium on Telecommunications*, pp. 59–64, Dec 2010.

[13] Y. Xu, Z. Wang, P. Liu, J. Chen, S. Han, C. Yu, and J. Yu, "Accuracy analysis and improvement of visible light positioning based on vlc system using orthogonal frequency division multiple access," *Opt. Express*, vol. 25, pp. 32618–32630, Dec 2017.

[14] E. Shinwasusin, C. Charoenlarpnopparut, P. Suksompong, and A. Taparugssanagorn, "Modulation performance for visible light communications," in *2015 6th International Conference of Information and Communication Technology for Embedded Systems (IC-ICTES)*, pp. 1–4, March 2015.

[15] M. C. Perez, J. Urena, . Hernandez, A. Jimenez, and C. De Marziani, "Efficient Generation and Correlation of Sequence Pairs With Three Zero-Correlation Zones," *IEEE Transactions on Signal Processing*, vol. 57, no. 9, pp. 3450–3465, 2009.

[16] J.-H. Yan, Y.-J. Cheng, K.-H. Lin, D.-H. Chen, C.-J. Chen, and K.-M. Feng, "Multipath interference free multi-led visible light communications with gold sequence multiplexing," in *Optical Fiber Communication Conference*, Optical Society of America, 2018.

[17] E. Aparicio-Esteve, Á. Hernández, J. Ureña, J. M. Villadangos, and F. Ciudad, "Estimation of the Polar Angle in a 3D Infrared Indoor Positioning System based on a QADA receiver," *Proc. of 2019 International Conference on Indoor Positioning and Indoor Navigation (IPIN 2019)*, pp. 1–8, 2019.

[18] E. García, J. Ureña, J. J. García, M. C. Perez, F. D. Ruiz, C. Diego, and J. Aparicio, "Multilevel ls sequences with flexible zcz length and their application to local positioning systems," in *2012 IEEE International Instrumentation and Measurement Technology Conference Proceedings*, pp. 1665–1669, May 2012.

[19] Z. Zhang, "A flexible new technique for camera calibration," *IEEE Transactions on Pattern Analysis and Machine Intelligence*, vol. 22, no. 11, pp. 1330–1334, 2000.

[20] E. Olson, "Apriltag: A robust and flexible visual fiducial system," in *2011 IEEE International Conference on Robotics and Automation*, pp. 3400–3407, 2011.

[21] Y. Abdel-Aziz, H. Karara, and M. Hauck, "Direct linear transformation from comparator coordinates into object space coordinates in close-range photogrammetry," *Photogrammetric Engineering and Remote Sensing*, vol. 81, no. 2, pp. 103 – 107, 2015.

[22] I. Markovsky and S. Huffel, "Overview of total least-squares methods," *Signal Processing*, vol. 87, pp. 2283–2302, 10 2007.

[23] E. Aparicio-Esteve, Á. Hernández, and J. Ureña, "Evaluation of mai effect in encoding techniques for an infrared positioning system," *IEEE International Instrumentation & Measurement Technology Conference*, pp. 1–6, 2020.

[24] E. Aparicio-Esteve, Á. Hernández, J. Ureña, and J. M. Villadangos, "Visible Light Positioning System based on a Quadrant Photodiode and Encoding Techniques," *IEEE Transactions on Instrumentation & Measurement*, pp. 1–15, 2019.

[25] M. C. Pérez Rubio, *Generación y Correlación Eficiente de Códigos Binarios Derivados de Conjuntos de Secuencias Complementarias para Sistemas Ultrasónicos*. PhD thesis, Universidad de Alcalá, 2009.

[26] "Optitrack motion tracking system," [online] Available: https://www.optitrack.com/, 2020.

[27] F. S. Inc., "Series 6 data sheet quad sum and difference amplifier, part description qp50-6-18u-sd2, product specification," 2012.

[28] E. Aparicio-Esteve, l. Hernández, J. Ureña, J. M. Villadangos, S. Lluva, and M. C. Pérez-Rubio, "Detecting Relative Amplitude of IR Signals with Active Sensors and Its Application to a Positioning System," *Applied Sciences*, vol. 10, no. 18, 2020.